2021 43rd Annual International Conference of the
IEEE Engineering in Medicine & Biology Society (EMBC)
Oct 31 - Nov 4, 2021. Virtual Conference

Parylene Photonic Microimager for Implantable Imaging*

Jay W. Reddy, Mohammad H. Malekoshoaraie, Vahid Hassanzade, Ramgopal Venkateswaran, Maysamreza Chamanzar, *Member, IEEE*

***Abstract*— We have recently introduced a fully flexible, compact photonic platform, Parylene photonics. Here, we demonstrate a Parylene photonic waveguide array microimager with a light source localization accuracy of 17.04 µm along the x-axis and 30.07 µm along the y-axis over a 200 µm×1000 µm region. We show the feasibility of fluorescent imaging from mouse brain tissue using the microimager array.**

***Clinical Relevance*— Implantable microimagers can be used for clinical intraoperative monitoring as well as structural and functional imaging with cell-type specificity in research.**

I. Introduction

Optical techniques allow high spatial resolution structural and functional interrogation of biological tissue. In neuroscience, calcium imaging [1] and optogenetics [2] enable optical stimulation and recording of neural activity. However, the scattering and absorption of light in tissue limits optical access [3]. Therefore, implantable devices and endoscopic imaging techniques are desired to enable optical techniques in deep tissue.

Miniaturized microscopes (miniscopes) and optical fiber bundles have been used as implantable imagers. However, typical GRIN lenses used in miniscopes are millimeters in diameter and optical fiber bundles are typically large (diameter ~250 µm) [4,5]. Moreover, the brain tissue is vulnerable to damage from large rigid implants [6]. Therefore, compact, and flexible implantable devices are highly desired. We have recently demonstrated a fully flexible, compact waveguide platform using biocompatible polymers, Parylene C, and PDMS. [7]. Here, we present the design, fabrication, and experimental characterization of a Parylene photonic waveguide array microimager which can find intriguing applications for minimally invasive endoscopic imaging.

II. Methods

A. Design and Fabrication

The imager is implemented using an array of flexible Parylene photonic waveguides. The waveguide core is composed of Parylene C, a high refractive index biocompatible polymer (n = 1.639), which is transparent throughout the visible spectrum. PDMS is used as the waveguide cladding due to its lower refractive index than Parylene C (n = 1.4), providing a large index contrast (Δn = 0.239) to confine an optical mode. A unique feature of this platform design is the monolithic integration of embedded 45-degree micro-mirrors at the input and output ports, which enables broadband 90-degree input/output coupling of light. Therefore, the waveguide array imager is capable of light collection and readout from the surface, unlike traditional end-firing fiber bundle and GRIN lenses.

The devices are fabricated at the wafer scale using planar microfabrication techniques. The fabrication was performed based on a process reported in our previous work [7]. Briefly, anisotropic KOH etching of a Si wafer substrate is used to form a smooth mold surface for the 45-degree micro-mirrors. A 1 µm-thick PDMS layer is spin-coated as the waveguide cladding. Then, metal micro-mirrors are deposited via electron-beam evaporation and patterned via lithography and lift-off. Parylene C polymer is deposited as the waveguide core material and patterned using oxygen plasma reactive ion etching with a Cr hardmask. Finally, an upper cladding layer of 1 µm-thick PDMS is spin-coated to complete the waveguide structure. Multiple device size variants are defined on the same wafer via planar lithography.

The design of the waveguide array microimager is shown in Fig. 1. A 200 µm×1000 µm input region is connected to a symmetric output region by a long (1 cm) waveguide array. A 2D arrangement of 25 waveguide channels form individual pixels of the waveguide array microimager in the input and output regions. The input port to each waveguide is formed by the 5 µm× 30 µm micromirror. These input ports are staggered to accommodate routing of the individual waveguide channels.

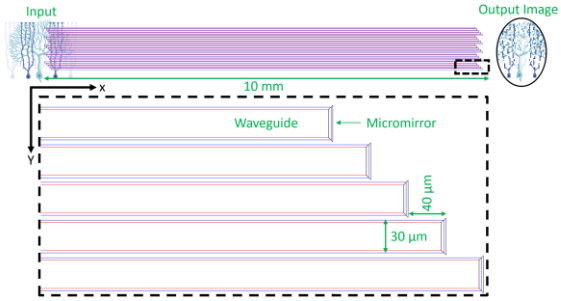

Figure 1. Schematic diagram of the waveguide array microimager.

*Research supported by the National Science Foundation under Grant No. 1926804 and National Institutes of Health under award No. 1RF1NS113303

J. Reddy is with the Department of Electrical and Computer Engineering, Carnegie Mellon University, USA (e-mail: jreddy1@andrew.cmu.edu)

M. Malekoshoaraie is with the Department of Electrical and Computer Engineering, Carnegie Mellon University, USA (e-mail: mohammam@andrew.cmu.edu)

V. Hassanzade is with the Department of Electrical and Computer Engineering, Carnegie Mellon University, USA (e-mail: vhassanz@andrew.cmu.edu)

R. Venkateswaran is with the Department of Electrical and Computer Engineering, Carnegie Mellon University, USA (e-mail: ramgopav@andrew.cmu.edu)

M. Chamanzar is with the Department of Electrical and Computer Engineering, Carnegie Mellon University, USA (email: mchamanzar@cmu.edu)

B. Characterization

To analyze the response of the Parylene photonic waveguide array imager, an optical fiber (P1-460Y-FC, ThorLabs) connected to a fiber-coupled laser source (LP633-SF50, ThorLabs) at λ = 633 nm was moved over the imager input port array while the output port array was imaged onto a CCD camera (EO-5012M, Edmund Optics) through a zoom lens (600i, Edmund Optics). The fiber position was controlled by a precision XYZ motorized micromanipulator (Patchstar, Scientifica). The exposure time of each image was automatically adjusted to keep the CCD camera sensor under saturation and maximize the dynamic range.

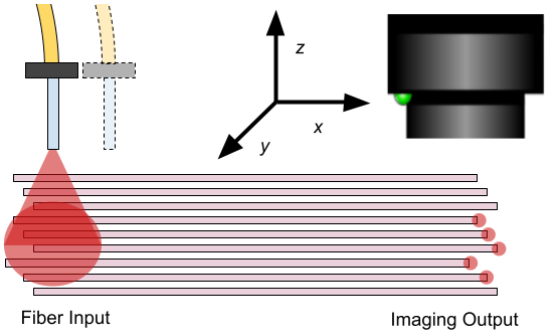

Figure 2. Imager characterization: A fiber is moved over the input port array while the output is detected through a CCD camera.

C. Analysis

Images captured by the CCD camera were analyzed using Python 3.8 and OpenCV 4.5.1. First, an image of the waveguide array imager output was captured with all output ports illuminated (Figure 3a). Individual output ports were detected by thresholding and circular regions of interest (ROIs) were defined around each identified output port. The CCD camera position was fixed during the entire experiment so that the position of each output port within the image did not change from image-to-image, and the same ROIs were used for all images. The relative intensity of each waveguide was measured by summing the pixel intensities within the circular ROI. Pixel intensities between different images were scaled by the exposure time from the image capture,

$$I_{scaled} = \frac{I_{raw}}{t_{exp}}.$$

A 5×5 matrix of waveguide output intensities was processed for each input condition (Figure 3b). Marginal distributions of the fiber intensity over the *x*- and *y*-axis were calculated by summing over the other axis:

$$I(x) = \sum_y I(x,y), I(y) = \sum_x I(x,y).$$

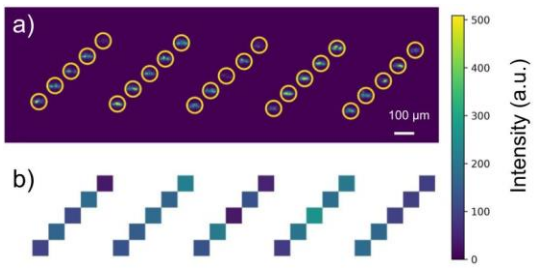

Figure 3. a) Individual waveguide regions of interest are circled. b) Analyzed waveguide array imager matrix showing pixel intensities.

The input fiber position along the *x*- and *y*-axis were estimated as the center of mass of the marginal intensity distributions:

$$\hat{x} = \frac{\sum_x xI(x)}{\sum_x I(x)}, \hat{y} = \frac{\sum_y yI(y)}{\sum_y I(y)}.$$

To estimate the noise of the center of mass estimate, a third-degree polynomial was fit to the data. The residual error of the polynomial model was used as a measure of the noise of the system, and the standard deviation (σ) of the noise was calculated. The peak sensitivity was defined as

$$sensitivity = \max\left(\frac{\partial \hat{x}}{\partial x}\right).$$

Then, the limit of detection (LOD) for a 95% confidence interval of the light source position is calculated as

$$\text{LOD} = \frac{4\,\sigma}{sensitivity}.$$

III. Results

A. Directional Sweep

The response of the waveguide array imager to optical fiber movements along the *x*-, *y*-, and *z*-axes were measured. First, the fiber was positioned above the center of the waveguide array and the intensity was measured as the fiber was withdrawn along the *z*-axis (Fig. 4a). The marginal intensity distribution along the *y*-axis (Fig. 4b) shows the downsampled 5-pixel reconstruction of the Gaussian beam profile of the fiber. As the fiber is moved farther from the waveguide array imager along the *z*-direction, the intensity of the fiber output beam is attenuated, and the beam width is increased as the beam diverges.

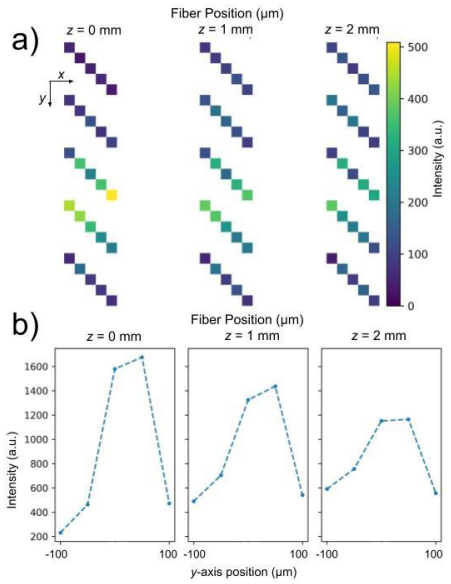

Figure 4. a) Waveguide array imager response to a fiber sweep along the *z*-axis. b) *y*-axis marginal intensity distribution showing the gaussian beam profile of the fiber. The beam is attenuated and spread as the fiber is moved further from the input port.

Next, the waveguide array imager response was measured as the fiber was swept along the *y*-axis (Fig. 5). Although the peak intensity of the fiber beam should not change as it is moved in the imaging plane, the imager output shows different

peak intensities depending on the location, due to the differing sensitivities of individual pixels from fabrication variation.

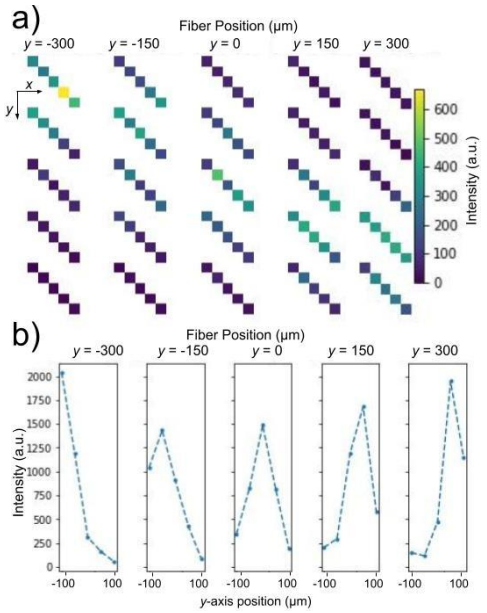

Figure 5. a) Waveguide array imager response to a fiber sweep along the *y*-axis. b) *y*-axis marginal intensity distribution showing the gaussian beam profile of the fiber. The center of the intensity distribution moves as the waveguide is swept in the *y*-direction.

Lastly, the waveguide array imager response along the *x*-axis was measured (Fig. 6). The *x*-axis pixel spacing is smaller than the spacing along the *y*-axis. As a result, the fiber beam profile is sampled over a smaller interval and the edge-to-edge variation of the underlying signal is reduced. The fiber distribution looks flatter overall along the *x*-axis, and variations in pixel intensity become more prominent, since there is less variation in the underlying signal.

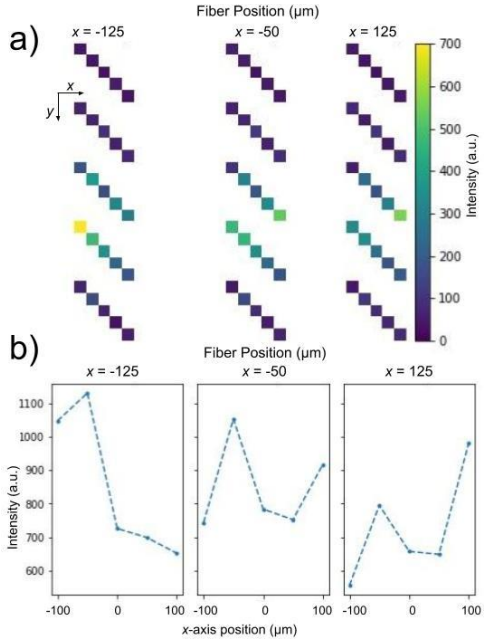

Figure 6. a) Waveguide array imager response to a fiber sweep along the *x*-axis. b) *x*-axis marginal intensity distribution showing the gaussian beam profile of the fiber. The center of the intensity distribution moves as the waveguide is swept in the *x*-direction.

B. *Source Localization*

Ultimately, the purpose of an imager as opposed to a photometer is to capture spatial information about light sources in a scene. To demonstrate this capability for the waveguide array microimager, we localize the optical fiber light source position in the *xy* plane based on the imager readout. We use the center of mass of the *x* and *y* marginal intensity distributions to estimate the fiber position in *x* and *y*. Figure 7 shows that the center of mass of the intensity distribution directly tracks the *x* and *y* position of the fiber across the imager. Both estimates saturate as the fiber position exceeds the limits of the imager (+/- 100 μm in *x*, +/-500 μm in *y*) (Fig. 7). As the fiber beam location extends beyond the edge of the imager array, the center of mass estimate does not receive information beyond the extents of the imager. Therefore, the sensitivity of the imager to a change in fiber location is reduced near the edges of the imager array. Based on the peak sensitivity at the center of the array, we calculate an LOD of the waveguide array imager was 17.04 μm along the *x*-axis and 30.07 μm along the *y*-axis.

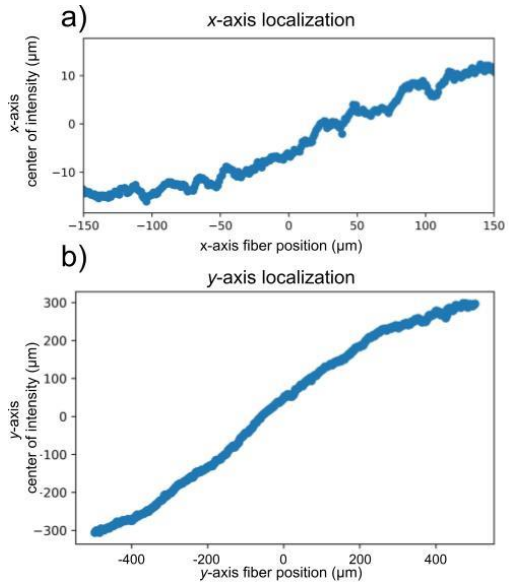

Figure 7. a) Fiber position localization via center of intensity along the *x*-axis. b) Fiber position localization via center of intensity along the *y*-axis.

C. *Fluorescent Imaging of a Brain Slice*

To demonstrate sufficient sensitivity of the imager to perform biological imaging, we placed a fluorescently-stained mouse brain slice (AlexaFluor 647, ThermoFisher) above the microimager and a long-pass ($\lambda > 650$ nm) emission filter (FEL0650, ThorLabs) in the output imaging path of the setup shown in Figure 2. A more sensitive CCD camera (CC505MU, ThorLabs) was used to detect the fluorescence emission. Fluorescent imaging was performed by moving the brain slice along the *y*-direction with steps of 127 μm. The images in Fig. 8a show the fluorescent images of the brain slice taken with the microimager alongside an image of the stained brain slice taken using a benchtop microscope. The micromimager can detect the fluorescence emission and the average intensity corresponds to the fluorophore concentration in the imager field of view. Fig 8b shows the imager can detect the boundary

of the brain slice when the sample is partially and then completely moved away from the field of view.

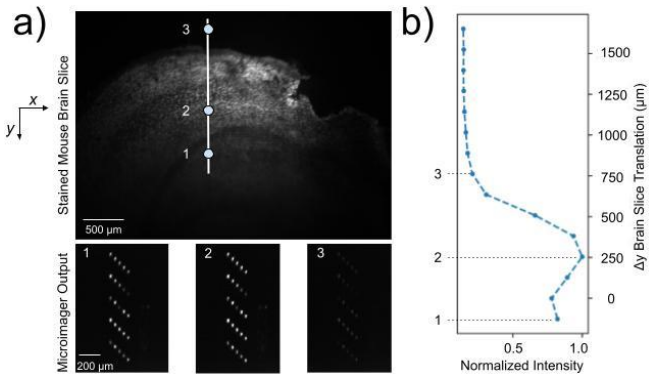

Figure 8. a) Fluorescent microscope image of Alexa Fluor-stained mouse brain tissue slice, with inset images of the microimager readout at various locations of the tissue. b) Normalized average intensity of the microimager output versus position on the tissue.

IV. Discussion

We have demonstrated that a 5×5 array of Parylene photonic waveguides can be used for imaging. The accuracy of the waveguide array was characterized by imaging an input optical fiber. We also demonstrated proof-of-concept fluorescent imaging of mouse brain tissue stained with Alexa Fluor 647. The preliminary results show that it is possible to image the boundaries of the brain tissue slice.

It should be noted that some waveguide outputs are dimmer than others. The waveguide-to-waveguide variability stems from the fabrication imperfections and results in distortion of the input image. These variations can be accounted for by calibrating the individual waveguides before imaging. Two feasible calibration procedures would be to either measure the response of each waveguide pixel to a uniform light source, or sequentially illuminate each waveguide pixel and measure the output intensity.

Here, we showed a proof-of-concept imager with only 25 waveguide pixels. However, the waveguide routing uses a very conservative pitch of 40 µm. Parylene photonic waveguides have been demonstrated with sizes as small as 10 µm [8], so simple lithographic scaling will allow a moderate increase to at least 100 waveguide imager pixels. The single-layer routing of the current imager design requires a linear increase in routing space for each pixel, which puts a fundamental limit on the number of pixels and the maximum pixel density. Scaling beyond a few hundred pixels in the waveguide imager array will require additional planer routing layers, or photonic switches to form an integrated multiplexer which can allow multiplexed addressing of many more output ports. Even with a modest number of pixels, the spatial resolution of the microimager demonstrated here can be useful in biological studies, for example for in-vivo fluorescent imaging.

Acknowledgment

J.W.R. acknowledges support by the Carnegie Mellon University Ben Cook Presidential Graduate Fellowship, the Carnegie Mellon University Richard King Mellon Foundation Presidential Fellowship in the Life Sciences, the Axel Berny Presidential Graduate Fellowship, and Philip and Marsha Dowd. Figure 1 illustration created with BioRender.com.

References

[1] R. A. de Melo Reis, H. R. Freitas, and F. G. de Mello, "Cell Calcium Imaging as a Reliable Method to Study Neuron–Glial Circuits," *Frontiers in Neuroscience*, vol. 14. Frontiers Media S.A., Oct. 02, 2020, doi: 10.3389/fnins.2020.569361.

[2] C. K. Kim, A. Adhikari, and K. Deisseroth, "Integration of optogenetics with complementary methodologies in systems neuroscience," *Nature Reviews Neuroscience*, vol. 18, no. 4. Nature Publishing Group, pp. 222–235, Apr. 01, 2017, doi: 10.1038/nrn.2017.15.

[3] V. Ntziachristos, "Going deeper than microscopy: The optical imaging frontier in biology," *Nature Methods*, vol. 7, no. 8. Nature Publishing Group, pp. 603–614, 2010, doi: 10.1038/nmeth.1483.

[4] B. A. Flusberg, E. D. Cocker, W. Piyawattanametha, J. C. Jung, E. L. M. Cheung, and M. J. Schnitzer, "Fiber-optic fluorescence imaging," *Nature Methods*, vol. 2, no. 12. pp. 941–950, Dec. 2005, doi: 10.1038/nmeth820.

[5] G. Oh, E. Chung, and S. H. Yun, "Optical fibers for high-resolution in vivo microendoscopic fluorescence imaging," *Optical Fiber Technology*, vol. 19, no. 6 PART B, pp. 760–771, 2013, doi: 10.1016/j.yofte.2013.07.008.

[6] A. Lecomte, E. Descamps, and C. Bergaud, "A review on mechanical considerations for chronically-implanted neural probes," *Journal of Neural Engineering*, vol. 15, no. 3. Institute of Physics Publishing, Mar. 05, 2018, doi: 10.1088/1741-2552/aa8b4f.

[7] J. W. Reddy, M. Lassiter, and M. Chamanzar, "Parylene photonics: a flexible, broadband optical waveguide platform with integrated micromirrors for biointerfaces," *Microsystems and Nanoengineering*, vol. 6, no. 1, Dec. 2020, doi: 10.1038/s41378-020-00186-2.

[8] J. W. Reddy, M. H. Malekoshoaraie, M. Lassiter, and M. Chamanzar, "Parylene photonics: A flexible, biocompatible, integrated photonic system for optical monitoring and stimulation of deep tissue," in *Integrated Sensors for Biological and Neural Sensing*, Mar. 2021, vol. 11663, p. 33, doi: 10.1117/12.2577918.